Materials Science & Engineering A 770 (2020) 138522

Contents lists available at ScienceDirect

Materials Science & Engineering A

journal homepage: http://www.elsevier.com/locate/msea

Microstructure of intercritical heat affected zone and toughness of microalloyed steel laser welds

L.S. Derevyagina [a,*], A.I. Gordienko [a], A.M. Orishich [b], A.G. Malikov [b], N.S. Surikova [a], M. N. Volochaev [c]

[a] Institute of Strength Physics and Materials Science of Siberian Branch Russian Academy of Sciences, 2/4, pr. Akademicheskii, Tomsk, 634055, Russia
[b] Khristianovich Institute of Theoretical and Applied Mechanics of the Siberian Branch of the Russian Academy of Sciences, 4/1, Institutskaya str., Novosibirsk, 630090, Russia
[c] Kirensky Institute of Physics of the Siberian Branch of the Russian Academy of Sciences (SB RAS), Akademgorodok 50, bld. 38, Krasnoyarsk, 660036, Russia

ARTICLE INFO

Keywords:
Low-carbon steel
Laser welding
Heat affected zone
Structure
Toughness

ABSTRACT

Microstructure of laser welds of the X70 low-carbon pipe steel was studied. High cooling rates after laser welding and non-uniform distribution of carbon in the ferrite-pearlite base metal caused formation of regions with increased microhardness (up to 650 HV) in inter-critical heat affected zone (ICHAZ). These regions consisted of finely dispersed degenerate upper bainite and martensite-austenite constituents of a slender shape and small fraction of a massive shape along the boundaries of bainite laths, as well as twinned martensite. High concentration of martensite-austenite constituents (10–16%) and residual stresses in ICHAZ, as well as a dendritic martensitic structure with carbide interlayers along the boundaries of martensite laths in fusion zone were the main reasons of sharp decrease in charpy impact energy of the welded samples. High microhardness of the laser welds was decreased down to 320 HV and their brittleness was improved by annealing. Also, in ICHAZ, degenerate upper bainite and the regions of martensite-austenite constituents decayed forming tempered sorbite and Fe_2C and Fe_3C carbides, respectively. Charpy impact energy of the welds doubled after annealing compared to the welds without annealing, and ductile-brittle transition temperature decreased down to –60°C.

1. Introduction

It is known that special types of thermo-mechanical treatment improve operational properties of low carbon microalloyed pipeline steels [1–5]. However, high strength and fracture toughness of pipes significantly reduce after welding [6]. This is due to the fact that inhomogeneous gradient structures are formed in welded joints during rapid heating and subsequent cooling. Welded metal includes many types of intermediate transformation structures such as granular bainite, upper and lower bainite, martensite, martensite-austenite (M-A) constituent, dispersed particles of second phases, etc. As a result, composition and conditions for formation of intermediate microstructures of the welded metal determining its properties is an important research task.

Submerged arc welding is one of the main technological operations in the manufacture process of pipes [6–8]. However, this method has a significant drawback because of large heat input extends heat affected zone (HAZ) and decreases mechanical properties [7]. An alternative welding process is laser welding [9–13]. This technology is more efficacious than conventional welding methods. In addition, width of fusion zone (FZ) and HAZ is much smaller compared to other welding methods. This is due to the fact that energy of a laser beam is concentrated on a tiny heating area [9,10,13]. Strength of laser welded joints of low carbon steels remains at the level of strength of the base metal [13]. However, the laser welds have a higher level of hardness because of high cooling rates [9,10].

In Refs. [11–13], it was shown that HAZ structures of laser welded joints included several different regions. The structures of these regions were determined by the maximum temperature to which they had been heated, as well as subsequent cooling rates. Their classification was generally similar in most papers, but there were some differences in terminology. Coarse-grained HAZ (CGHAZ) [11,12] or supercritical HAZ [13] was adjacent directly to FZ. It had been heated to a temperature significantly above the critical point Ac_3. Fine-grained HAZ (FGHAZ) and inter-critical HAZ (ICHAZ), in which the heating interval had been between A_{c3} and A_{c1}, followed it. Then, there was sub-critical HAZ (SCHAZ) which had been heated to a temperature below A_{c1}. It is

* Corresponding author.
E-mail address: lsd@ispms.tsc.ru (L.S. Derevyagina).

https://doi.org/10.1016/j.msea.2019.138522
Received 21 August 2019; Received in revised form 4 October 2019; Accepted 5 October 2019
Available online 9 October 2019

possible to control dimensions of these regions, their phase composition and morphology by changing the main parameters of laser welding (beam power and welding speed). However, few results of detailed studies of HAZ structures of laser welded pipe steels and data on their relationship with mechanical properties have been published to date. In this regard, the aim of this paper was to study the laws governing formation of HAZ in laser welded joints of the low-carbon steel and evaluate their mechanical properties.

2. Experimental procedure

The X70 low-carbon micro-alloyed pipeline steel was investigated. Its chemical composition is shown in Table 1. Plates to be welded were cut from a hot-rolled sheet with a thickness of 56 mm perpendicular to the rolling direction. Butt joints were welded using a 'Siberia-1' automated laser technological facility including a continuous CO_2 laser with a power of up to 8 kW [14]. Helium was used to protect the weld pool and the root. Initially, the parameters of the welding process were optimized (laser beam power *P*, welding speed *V*, and location of the focal spot *Δf* relative to the upper surface of the plates). The quality criterion was formation of welds without any visible discontinuities such as surface pores, lack of fusion and cracks. The plates were joined in one pass using the keyhole welding mode. The optimal welding parameters and dimensions of the plates of two types are shown in Table 2. Finally, some samples were annealed after welding at a temperature of 550 °C for 1 h.

Samples for metallographic study were prepared by the standard procedure followed by etching with 3% nital solution. Microstructure was investigated using a 'Zeiss Axiovert 25' optical microscope (OM), a 'LEO EVO 50' scanning electron microscope (SEM), a 'Philips CM-12' transmission electron microscope (TEM) as well as an 'HT-7700' TEM. An average grain size was determined from OM и TEM images using the linear intercept method. Concentration distribution of elements in the welds was evaluated by energy dispersive microanalysis using the 'LEO EVO 50' microscope. An 'FIB2100' focused ion beam (FIB) system was used for foil cutting and subsequent local study of HAZ structures. A scheme of foil cutting is shown in Fig. 1.

Microhardness was measured on the etched cross-sections of the samples along the horizontal axis of the welds using a 'PMT-3' microhardness tester. Load was 100 g, holding time was 10 s. At least 5 measurements were taken at each test point. Dimensions of the main part of the welded samples were 15 × 3×1 mm for mechanical static tensile tests using a Polyany type installation. Impact bending tests of specimens with a V-shaped notch were carried out using an 'INSTRON MPX 450' pendulum impact testing system in the temperature range T_{test} from +20 to –70 °C. Dimensions of the base metal samples were 10 × 10×55 mm; the welded samples were 8 × 3×55 mm. Only a qualitative assessment of fracture toughness was determined due to the different sizes of the samples. The notches crossed both FZ and HAZ. The fracture surfaces of the samples were investigated using a 'Philips SEM 515' SEM. Based on the results of the impact tests, the ductile-brittle transition temperature (DBTT) was determined. It corresponded to the mean value of the upper and lower shelf impact energy (USE and LSE). Also, the fracture appearance transition temperature corresponding to 50% ductile fracture ($FATT_{50}$) was estimated due to the fact that it was not possible to accurately measure of the USE and LSE boundaries [15].

Table 2
Plate dimensions and main laser welding parameters.

Specimen type	Plate dimensions, mm	P, kW	V, m/min	Δf, mm
Type I (for tensile tests)	55 × 55 × 1.2	1.2	1	–2
Type II (for impact bending tests)	55 × 55 × 3	2.2	1	–3

3. Results

3.1. Microstructures

The structure of the hot-rolled base metal of the X70 steel consisted of alternating ferrite and pearlite strips (Fig. 2a). The average ferrite grain size was 12 μm. VC vanadium carbides with sizes of 5–25 nm were found in ferrite grains (Fig. 2b). Area fraction of pearlite grains was about 20%. Their microstructure included alternating plates of ferrite and cementite (Fig. 2c and d). Thickness of ferrite plates was in the range of 100–300 nm, and cementite was in the range of 35–150 nm.

Width of the welds was 2.22 mm including FZ 1.22 mm wide and HAZ 1.00 mm wide (Fig. 3a). A dendritic structure including typical martensite laths was formed in FZ due to high cooling rates (Fig. 3b; Fig. 4a). Martensite colonies located both to the left and to the right of the weld axis at an angle of about 45°. Width of the martensite laths varied from 80 to 700 nm. Between the martensite laths, cementite inclusions in the form of thin interlayers with a width of 20–40 nm were found (Fig. 4c and d). More dispersed cementite plates with a thickness of 5–10 nm were inside wide martensite laths across the plates (Fig. 4b). High dislocation density was found in martensitic laths (Fig. 4b).

The two main regions (FGHAZ and ICHAZ) were found in HAZ (Fig. 3a). FGHAZ with a width of only 150–200 μm adjoined directly to both sides of FZ. FGHAZ had a transitional structure of upper bainite and martensite. Bainite and martensite plates were bounded by the boundaries of former austenitic grains. This fact indicated that this zone had been heated to the temperature range of the γ-phase existence above the critical point A_{c3}.

ICHAZ occupied the main area of HAZ. Its structure consisted of alternating strips of light ferrite regions ('A' and 'B', Fig. 3c) and darker regions ('C' and 'D', Fig. 3c). The 'C' and 'D' regions abruptly transformed into the pearlite phase in the base metal (BM). Two regions were distinguished in ICHAZ. They differed in fineness of ferrite grains ('A' and 'B', Fig. 3c), as well as a darker and lighter shade of the 'C' and 'D' regions. Mean size of ferrite grains was approximately 12 μm in BM and in the areas adjacent to BM. Small ferrite grains of non-equiaxed shape with an average size of about 4 μm were in the areas closer to FZ.

Harnessing of the FIB system made it possible to study in detail the structure of HAZ in the 'C' and 'D' regions (the foil cutting scheme is shown in Fig. 1). The 'D' region had an inhomogeneous structure (Fig. 5a). According to the classification [16], the structure consisted of predominantly degenerate upper bainite (DUB) and a small fraction of granular bainite (GB) (Fig. 5b and c) in a lighter zone 1 (Fig. 5a) adjacent to the 'B' ferrite region. DUB had a lath-type morphology of ferrite with M-A constituent at the boundaries of bainite laths (Fig. 5d and e). Two types of M-A constituent with slender and massive (or blocky-type) shapes were in the structure, similar to what the authors of [17–19] had observed. Thickness of M-A constituent plates of a slender shape was in the range of 20–60 nm; their length was in the range of 120–400 nm. Width of M-A constituent plates of a massive shape was 80–120 nm. Small areas of twinned martensite were also in the structure (Fig. 5f–h).

Table 1
Chemical composition of the X70 pipeline steel.

Element	C	Mn	V	Nb	Si	Ti	Cu	Al	P	S
Composition (wt, %)	0.13	1.6	0.05	0.04	0.4	0.05	0.3	0.03	0.013	0.01

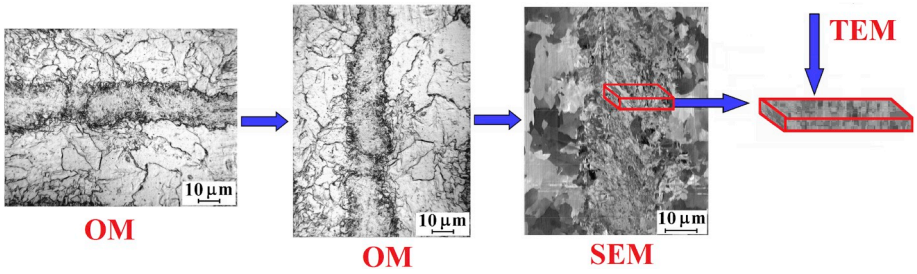

Fig. 1. Scheme of foil cutting by a focused ion beam.

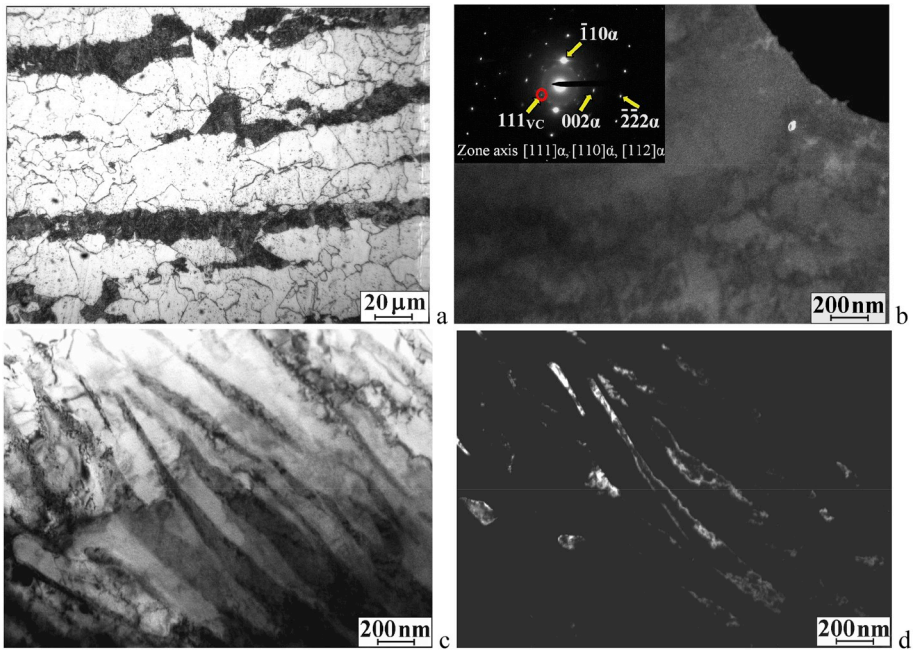

Fig. 2. Microstructure of the base metal: optical micrograph (a), TEM images (b–d): dark-field image in the <111> reflection of carbide VC (b): the diffraction pattern shows the $[111]_\alpha$, $[110]_\alpha$, $[112]_\alpha$ zone axis reflections, the red circle indicates the <111> reflections of carbide VC; bright-field image in a pearlite grain (c) and dark-field image in the <200> reflection of carbide Fe_3C (d). (For interpretation of the references to colour in this figure legend, the reader is referred to the Web version of this article.)

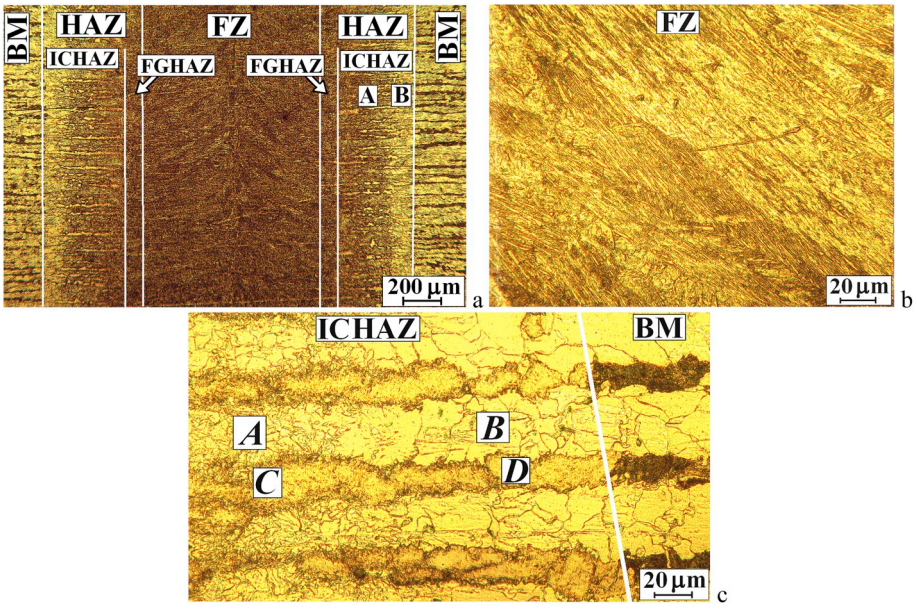

Fig. 3. Optical micrographs of the welded metal: macroimages of the weld (a), FZ (b), and HAZ (c).

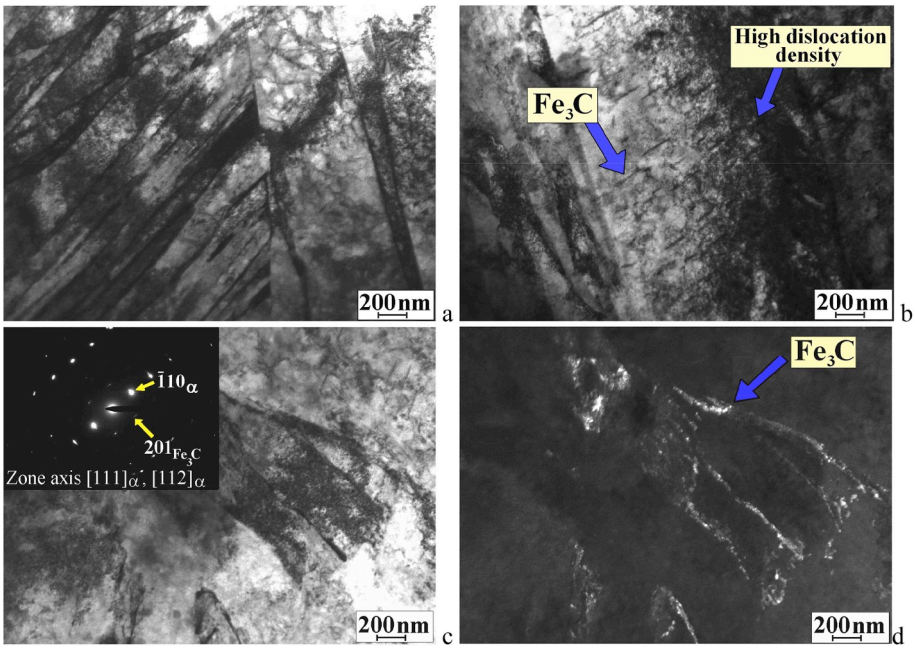

Fig. 4. TEM images of FZ: bright-field images (a–c); dark-field image (d) in the <201> reflection of Fe_3C carbide (indicated by the arrow on the diffraction pattern in Fig. 4c).

The reflection from the twin is indicated by an arrow in the microdiffraction pattern (Fig. 5h), and the trace of the twinning plane is highlighted by a dashed line. Width of dispersed plates in twinned martensite was 5–7 nm. Dimensions of the structural constituents of the studied steel are shown in Table 3 for comparison.

The zone 1 was followed by a darker zone 2 (Fig. 5a) with a lath structure (Fig. 6a). Width of lighter laths in the zone 2 ranged from 140 to 250 nm. These values were comparable to width of laths in the zone 1 but less than martensite laths in FZ (Table 3). Between these light laths, dark laths located which included austenite (Fig. 6b). Two zones of α- and γ-phases are presented in the microdiffraction pattern (рис. 6d). This fact indicates that the dark areas were M-A constituent of a slender shape (or elongated rods [19]). The structure of M-A constituent was heterogeneous in the form of a thin lamellar structure (Fig. 6c). Thickness of the M-A constituent areas was in the range of 15–50 nm and length was 100–800 nm. Such structure is not typical for martensitic lamellas. Therefore, it was interpreted as degenerate upper bainite in accordance with the classification [16]. Reflections from carbide particles were absent in the electron diffraction patterns obtained from the zones 1 and 2.

The boundaries of the 'C' region in HAZ were darker than the 'D' region in optical images (Fig. 3c). Apparently, carbon precipitated at the grain boundaries in carbon-rich areas and cementite particles were formed. The results of energy dispersive analysis confirmed this fact (Fig. 7, Table 4). The carbon content was 0.6% in the 'B' ferrite region (spectrum 1) but increased up to 1.5–2.0% in the 'D' carbon enriched region (spectrums 2–4). At the boundaries of the 'C' region, carbon content increased significantly up to 4–10% (spectrums 6–8). Carbon content in the center of the 'C' region (spectrum 5) was about 2%.

After annealing, no qualitative changes occurred in FZ of the welded samples. They had the same dendritic structure (Fig. 8a and b). Width of martensitic laths did not change significantly after annealing. However, part of the martensite laths became lighter after annealing (Fig. 9a, regions I and II). This indicated that dislocation density decreased. Twinned martensite as well as Fe_2C and Fe_3C particles were found in some areas (Fig. 9b and c). It is known that Fe_2C particles are formed in martensite during annealing. This structure is typical for tempered martensite.

More significant structural changes occurred in HAZ. In ICHAZ, a banded structure and grain size difference in the ferritic regions were found (Fig. 8c). However, compared with the welded metal without annealing, there was an increase in dimensions of ferrite grains in the 'A*' and 'B*' regions to an average size of 8 and 20 μm, respectively. The 'C*' and 'D*' regions were darker in optical images compared to the welded metal without annealing (Fig. 3c). In addition, there were small bright areas inside the 'C*' region (Fig. 8c).

Rounded ferritic grains 700–900 nm in size were found in the samples after annealing (Fig. 10a) when studying of the fine structure of the 'D*' region in the zone 1 adjacent to the 'B' ferrite region. Fe_3C inclusions in the form of thin plates or particles were inside these grains and along their boundaries (Fig. 10a and b). The laths structure was preserved in the zone 2 located closer to the center of the 'D*' region. Width of the laths was in the range of 110–250 nm (Fig. 10c). At the same time, the laths became lighter in comparison with the welded metal without annealing (Fig. 6a). In the diffraction pattern, there were no austenite reflexes but many cementite ones. A large number of Fe_3C particles in the form of elongated plates with a width of 20–40 nm and lenticular particles with a width of 40–60 nm were found in the areas where M-A constituent were previously located (Fig. 10d). Thus, M-A constituent decayed to Fe_3C carbide when annealing. The formed structure was such as tempered sorbite.

3.2. Microhardness

Microhardness of the base metal was 170 HV in ferrite regions and 235 HV in pearlite. Distribution of microhardness values in the weld metal was extremely heterogeneous (Fig. 11). They were significantly higher compared to the base metal. Mean values of microhardness in FZ increased up to 370 HV. The microhardness curve had peaks and a significant increase in values up to 640–670 HV in HAZ (Fig. 11, indicated by a black arrow). There were no peaks on the curve and distribution of values became more uniform after annealing. Microhardness values in FZ and HAZ decreased down to ~320 HV. However, small peaks in HV values remained in HAZ (Fig. 11, indicated by a white arrow).

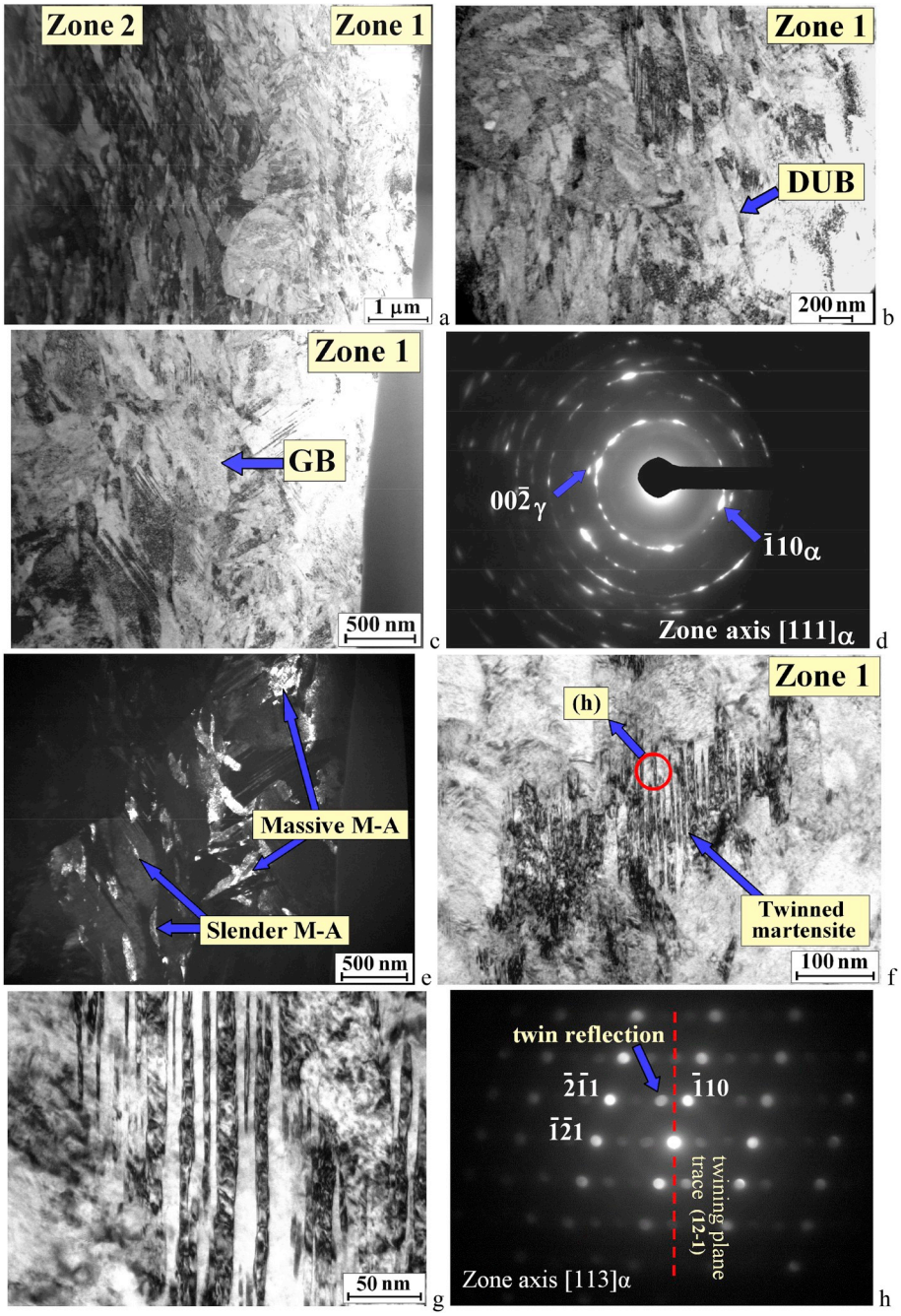

Fig. 5. TEM images of HAZ (region '*D*' according to Fig. 3c): general view of the foil (a), bright-field image in zone 1 (b–c) and corresponding diffraction pattern (d): the [111]α zone axis reflections indicated, the arrow points to the <00$\bar{2}$> reflection of γ-Fe; dark-field image in the <00$\bar{2}$> reflection of γ-Fe (e); bright-field image of twinned martensite (f, g) and selected area diffraction pattern for the region indicated by the red circle in Fig. 5f (h). (For interpretation of the references to colour in this figure legend, the reader is referred to the Web version of this article.)

3.3. Tensile behavior

Strength of the welded samples decreased slightly and was 93–95% of strength of BM (Fig. 12); ductility was about 85% of BM. After annealing, the mechanical characteristics of the welded samples changed insignificantly (ductility increased slightly). All welded samples had failure through BM.

3.4. Impact testing

Results of impact bending tests at room temperature showed that charpy impact energy of the welded samples was significantly less than the base metal samples (Table 5). At low T_{test}, charpy impact energy was critically low for all studied samples. DBTT and $FATT_{50}$ values of the base metal samples were slightly different (–32 °C and –18 °C, respectively). It was not possible to estimate DBTT of the welded samples because there were no accurate data on USE and LSE. However, almost the entire fracture surfaces of the welded samples had a brittle fracture pattern even at room temperature (Fig. 13a). Therefore, the $FATT_{50}$ was already at +20 °C.

Annealing of the welded samples made it possible to increase their charpy impact energy almost twice compared to the values without annealing (and even compared to the base metal at T_{test} below zero degrees Celsius). The fracture surfaces of the welded samples after annealing had a fully ductile manner at the temperature range down to –40 °C (Fig. 13b). On the fracture surfaces there were a large number of particles precipitated during tempering of martensite. Brittle manner of fracture was found only in the temperature range of –40 … –70°C. At the same time, DBTT and $FATT_{50}$ were in the range of –55 … –60 °C.

Table 3
Sizes of structural constituents in different zones of the weld and base metal.

Structural constituent	Width of structural constituents with lath morphology, nm			
	Pearlite in base metal	Welded joint		
		Fusion zone	Heat affected zone	
			Region *D*, Zone 1	Region *D*, Zone 2
α-lath morphology (ferrite, bainite, martensite)	100–300 (ferrite)	80–700 (martensite)	100–300 (bainite)	140–250 (bainite)
Cementite (Fe_3C) plates	35–150	Large 20–40, Small 5–10	–	–
M-A constituent	–	–	Slender 20–60 (length 100–400) Massive 80–120	Slender 15–50 (length up to 800 nm)
Twinned martensite plates	–	–	5–7	–

4. Discussion

During the process of laser welding of the X70 steel, solidification occurred from the edges of the weld pool to its center. Therefore, a columnar dendritic structure was formed in FZ during crystallization of grains. Mean values of microhardness of the metal in FZ increased up to 370 HV due to high cooling rates and formation of a lath martensitic structure. An increase in microhardness of the metal in FZ after laser welding up to 499 HV was also noted in Ref. [13].

Width of HAZ was 900–950 μm after laser welding. It was significantly less than after gas tungsten arc welding [9,10]. It should be noted that there was no CGHAZ. Apparently, this was due to high cooling rates. ICHAZ was the main region of HAZ (Fig. 3a). Location of the dark (with a high carbon content) and light (with a predominantly α-phase) regions in ICHAZ was as in BM. This indicates that ICHAZ had been heated to the temperature range when the two-phase (γ+α)-region existed. Different dispersion of light ferritic regions in ICHAZ (Fig. 3c, 'A' and 'B' regions) was due to different temperatures and cooling rates in these zones. Fining of ferrite grains in the 'A' region could be explained by the recrystallization process at elevated temperature because of its location next to FZ.

Carbon concentration was significantly higher in the 'D' region of ICHAZ (Fig. 3c), which corresponded to the former pearlite grains in the base metal (Table 4), in comparison with the 'B' neighboring ferrite region. A bainitic structure was formed in the 'D' region during subsequent fast cooling. GB and DUB were found in areas adjacent to ferritic

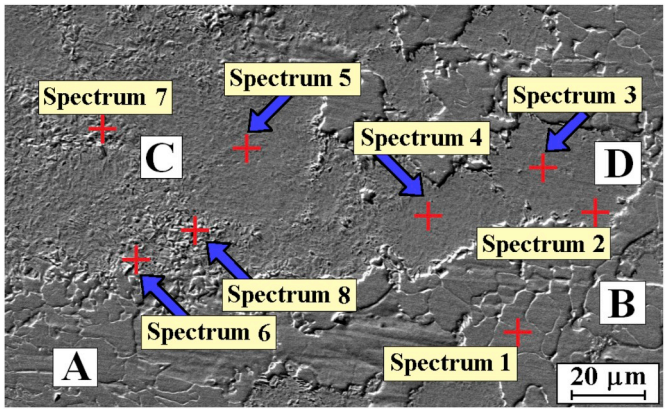

Fig. 7. SEM images of HAZ. Highlighted dots indicate areas where energy dispersive analysis was done; 'A', 'B', 'C', 'D' indicate the HAZ regions according to Fig. 3c.

Table 4
Elemental distribution in the HAZ of X70 steel, in wt %.

Spectrum	C	Si	V	Mn	Fe	Total
Spectrum 1	0.60	0.31		1.84	97.24	100.00
Spectrum 2	1.44			1.95	96.60	100.00
Spectrum 3	1.53	0.33		2.01	96.12	100.00
Spectrum 4	1.80	0.27		1.87	96.06	100.00
Spectrum 5	2.10	0.32		2.03	95.55	100.00
Spectrum 6	5.78	0.40		1.79	92.04	100.00
Spectrum 7	4.16	0.40		1.82	93.63	100.00
Spectrum 8	9.81	0.42	0.21	1.81	87.74	100.00

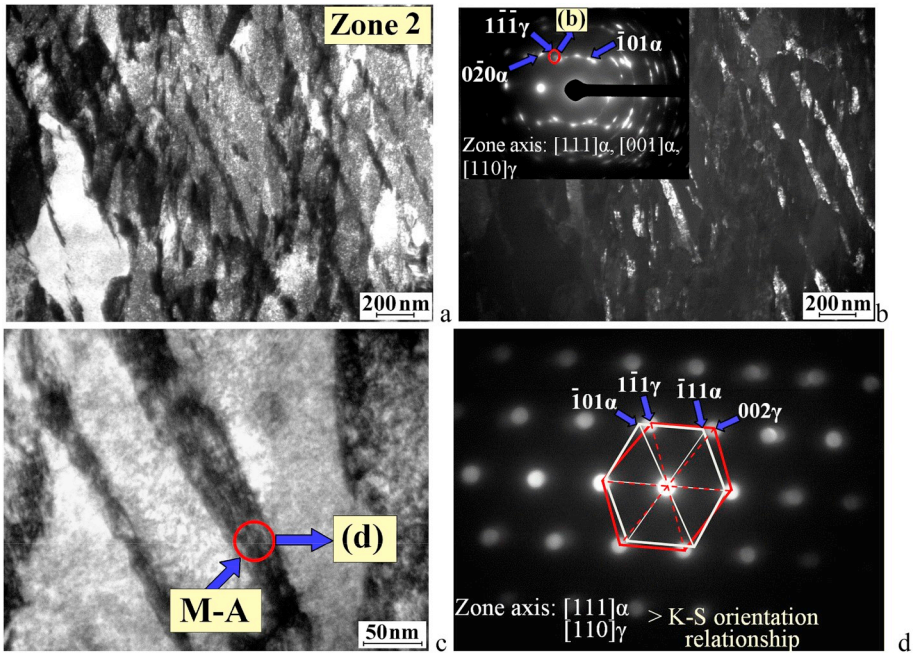

Fig. 6. TEM images of HAZ (zone 2 according to Fig. 5a): bright-field images (a, c), dark-field image in the <1$\bar{1}\bar{1}$> reflection of γ-Fe indicated by the red circle in the diffraction pattern, where the [111]α and [110]γ zone axis reflections are also highlighted (b); selected area diffraction pattern for the region indicated by the red circle in Fig. 6c, with the [111]α and [001]α zone axis reflections indicated (d). (For interpretation of the references to colour in this figure legend, the reader is referred to the Web version of this article.)

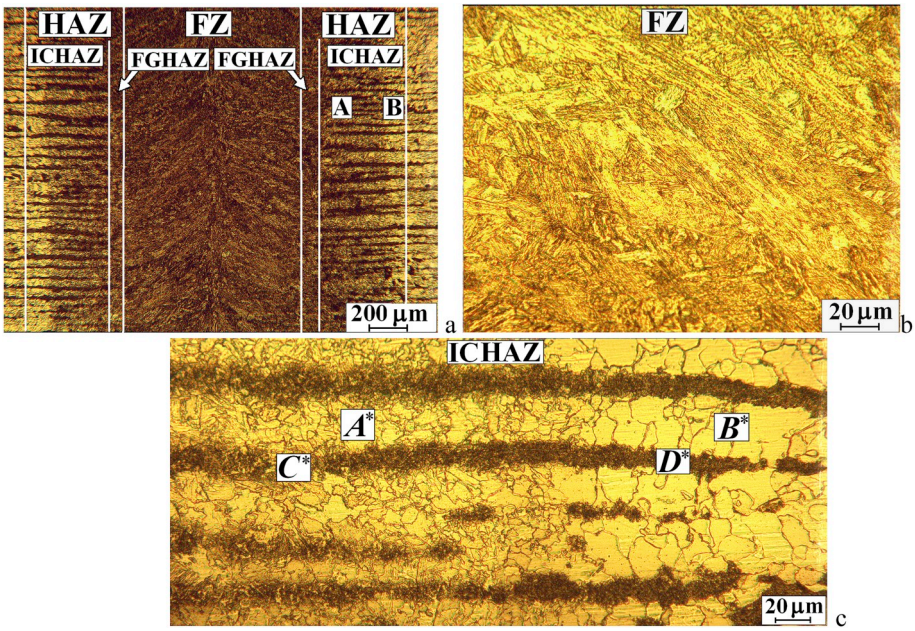

Fig. 8. Optical micrographs of the welded metal after annealing: macroimages of the weld (a), FZ (b), and HAZ (c).

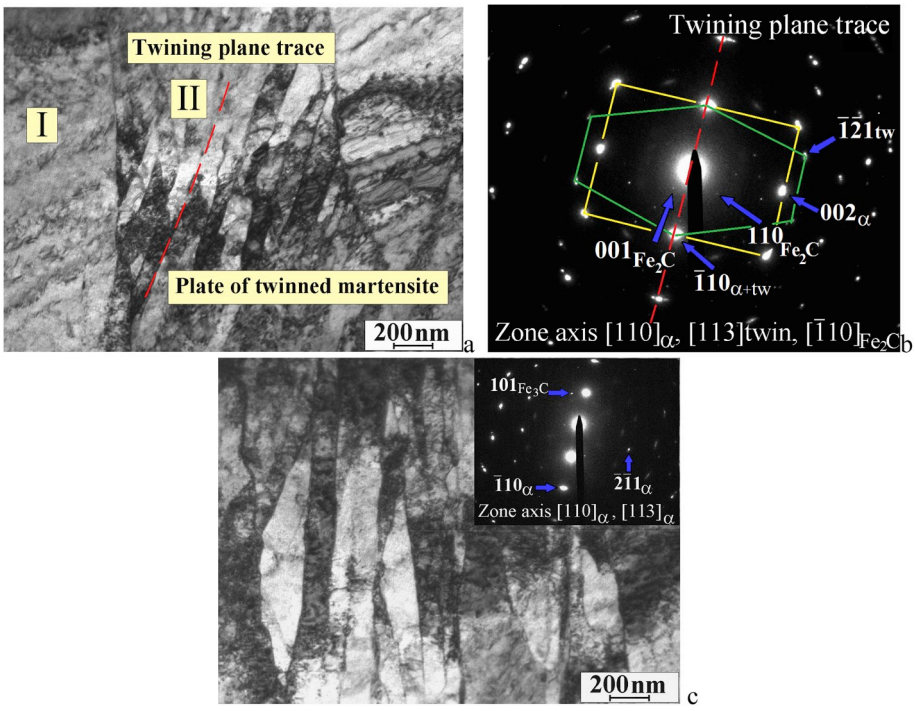

Fig. 9. TEM images of FZ of the weld after annealing: bright-field image (a) and corresponding diffraction pattern showing the [110]α, [113]twin, [-110]Fe_2C zone axis reflections (b), bright-field image and corresponding diffraction pattern showing the [110]α, [113]α zone axis reflections and <201> reflection of Fe_3C carbide (b).

grains (Fig. 5a, zone 1). Presence of GB in addition to DUB was due to the fact that carbon diffusion processes began in neighboring ferritic regions. Therefore, carbon concentration in austenite was partially reduced. In turn, this reduced its stability and shifting bainitic transformation into a range of higher temperatures. After laser welding, width of laths in DUB of ICHAZ was determined by width of lamellas in pearlite and had high dispersion of about 100–300 nm.

Dispersed areas of M-A constituent of slender and massive shapes (20–60 and 80–120 nm wide) were along the boundaries of the bainitic regions. Formation of M-A constituent was due to local high carbon concentration and high cooling rate. In Ref. [19], it was noted that M-A constituent of slender shapes (elongated rods) was formed at short cooling time and, accordingly, a higher cooling rate. As the cooling time increased, this changed into massive. M-A constituent in the form of twin martensite was also found in the structure. Not only an increased carbon concentration was necessary for its formation, but also inhomogeneity of carbon concentration inside austenite and thermal stresses in HAZ [20].

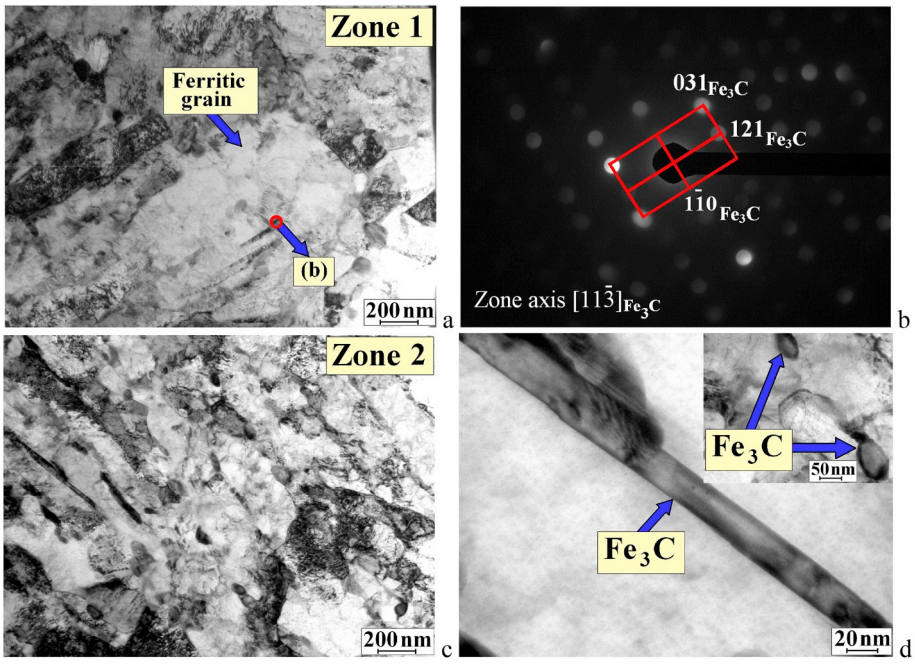

Fig. 10. TEM images of HAZ after annealing ('D*' region according to Fig. 8c): bright-field image in zone 1 (a), selected area diffraction pattern for the region indicated by the red circle in Fig. 10a (b); bright-field images in zone 2 (c, d). (For interpretation of the references to colour in this figure legend, the reader is referred to the Web version of this article.)

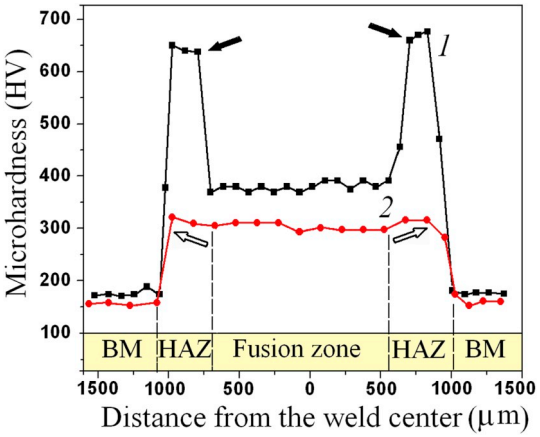

Fig. 11. Microhardness of the welded metal: 1 – without annealing; 2 – after annealing.

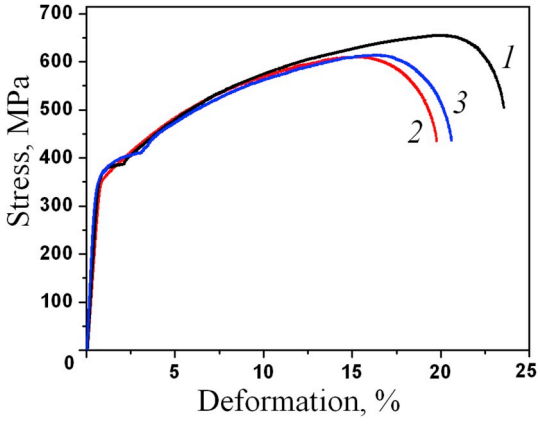

Fig. 12. Stress-strain curves of the X70 steel: base metal (1), welded metal (2) welded and annealed metal (3).

The diffusion processes had less time to complete in zone 2 of the 'D' region in ICHAZ (Fig. 5a) than in zone 1. Only DUB was present in the structure because carbon concentration in austenite was higher, its stability increased, and bainitic transformation was delayed. Areas of slender M-A constituent sections with a width of 15–50 nm located between DUB laths. Their length was greater than in zone 1. If we compare the pearlite structure of the base metal (Fig. 2c) with the structure in zone 2 (Fig. 6a), it can be seen that the bainitic structure inherited the structure of pearlite. This was because of high heating rate of the 'D' region did not allow to have uniform concentration of carbon in austenite. Thicknesses of ferrite laths in pearlite (100–300 nm) and laths in DUB (140–250 nm) were in approximately the same range of values. However, width of M-A constituent plates in DUB was significantly smaller than cementite plates in pearlite. This was the result of partial diffusion processes of carbon movement to neighboring ferrite regions. Thereby, volume fraction of M-A constituent in zones 1 and 2 was 10–16%. This was less than area fraction of pearlite in the base metal.

Table 5
Charpy impact energy of X70 steel.

Specimens	Charpy impact energy, J			DBTT, °C	$FATT_{50}$, °C
	T_{test} = +20 °C	T_{test} = –40 °C	T_{test} = –70 °C		
Base metal	200	20	11	–32	–18
Welded metal	20	10	4	–	+20
Welded and annealed metal	37	33	12	–55	–60

However, this was a rather large value; since it was shown in Ref. [17] that the area fraction of M-A constituent intercritically reheated coarse-grain HAZ (ICCGHAZ) was 3.7%. Ch. Li et al. showed [19], that amount of M-A constituent was related to a critical carbon content of residual austenite where the bainite or acicular transformation ceases. Consequently, heterogeneity in carbon concentration in the initial

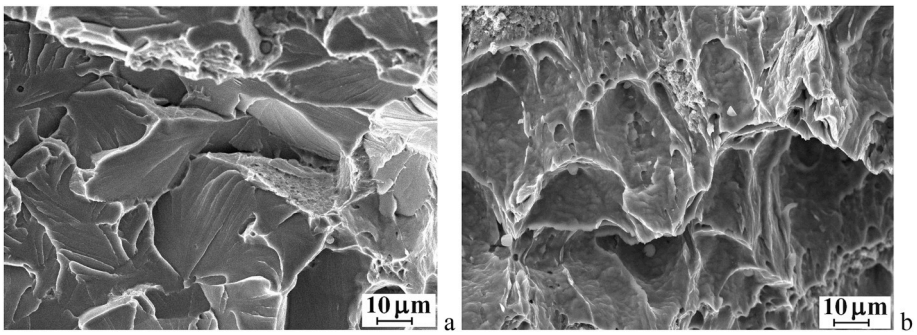

Fig. 13. Micrograph of the impact fracture surfaces of welded metal at +20°C (a) and welded and annealed metal at –40°C (b).

ferrite-pearlite structure caused formation of a large area fraction of M-A constituent.

The M-A constituent area had a lath structure (Fig. 6c) when thin plates of residual austenite alternated with martensite plates. Retained austenite had K–S orientation relationship with its neighboring martensite: $(-101)_M//(1-11)\gamma$ and $[111]_M//[011]\gamma$ (Fig. 6d) [21]. This indicates that it was the shearing mechanism of martensitic transformation.

Cooling rate of the metal in the 'C' region of ICHAZ was lower than in the 'D' region (Fig. 3c) and the temperature range, to which it had been heated, was higher because of its location next to FZ. In Ref. [19], it was also noted that distribution of carbon concentration in the interface was different according to change in cooling time. Therefore, at the boundaries of the 'C' region, diffusion processes of carbon precipitation were more intense and cementite particles were formed during subsequent fast cooling. However, the central zones of the 'C' region in ICHAZ also contained DUB and interlayers of M-A constituent. This caused high microhardness in these areas with only a slight decrease in their values (Fig. 11, indicated by black arrows). Thus, increase in microhardness in ICHAZ up to 640–670 HV was due to formation of fine laths in DUB with interlayers of M-A constituent. In Ref. [11], similar peaks in the microhardness curve were observed in FGHAZ after laser welding. They were associated with the effect of hardening due to a fine-grained structure in these areas. In our investigation, the greater microhardness in ICHAZ compared to FZ was associated with higher carbon concentration and greater dispersion of DUB laths compared to the martensite laths in FZ as well as formation of M-A constituent.

Microhardness values in FZ and ICHAZ exceed the level set by the standard DNV–OS–F101 for low-carbon steels ($HV \leq 325$) so dramatically reduced cold cracking resistance. In addition, heterogeneous distribution of microhardness in welds was also undesirable from the point of view of obtaining sufficient fracture toughness. Significant decrease in toughness and brittle fracture of the studied laser welded samples of the X70 steel was due to formation of a dendritic martensitic structure as well as carbide interlayers along the boundaries of martensite laths and between them in FZ. An additional problem was presence of DUB regions and high residual stresses in ICHAZ as well as a large proportion of M-A constituent. The authors of a large number of papers [18–20,22] showed that fracture toughness depended on sizes, volume fraction and shapes of M-A constituent. Impact strength decreased significantly when M-A constituent areas were massive due to large initial austenitic grains [22]. It is also known that the greater proportion of M-A constituent, the lower charpy impact energy [20]. The authors of [18,19,23] showed that M-A constituents of a slender shape included high carbon content were more harmful to toughness compared with massive ones. Microcracks formed by debonding of massive M-A constituent from a matrix or cracking propogation through slender M-A constituent caused brittle failure micromechanism [17,18,24]. It was also noted that formation of twinned martensite in HAZ was more detrimental to toughness [25]. Thus, large area fraction of slender M-A constituent and twinned martensite formed in the X70 steel welds caused significant decrease in charpy impact energy. Therefore, some welds were annealed.

Partial decay of the martensitic structure was in FZ after annealing. Mitigation of tetragonality occurred in the martensite lattice because of precipitation of Fe_2C and Fe_3C carbides and decrease in carbon content. Microhardness decreased down to 300 HV in FZ due to partial stress relaxation. A similar decrease in tempered martensite microhardness in SCHAZ was observed by the authors of [26]. Decay of DUB and formation of tempered sorbite occurred in ICHAZ. M-A constituent decayed and Fe_3C carbides formed. Because of this, the microhardness curve smoothed and distribution of values became more uniform (Fig. 11). Moreover, fracture toughness and cold resistance improved compared to the samples without annealing, and even compared to the base metal at low temperatures. The reasons for low ductility and cold resistance of hot rolled X70 steel were discussed in Refs. [27,28]. Whereas, in [29] it was shown that the decomposition of M-A constituents, formation of cementite and softening of bainitic matrix after tempering had resulted in higher density of microvoids and substantial plastic deformation before impact failure.

Thus, high values of microhardness and brittleness of the X70 steel laser welds can be partially decreased by annealing.

5. Conclusions

1. High cooling rates after laser welding and non-uniform distribution of carbon in the base metal of the X70 ferrite-pearlite steel caused formation of regions with increased microhardness (up to 650 HV) in ICHAZ. High microhardness was due to formation of finely dispersed DUB regions and M-A constituents of a slender shape and small fraction of a massive shape along the boundaries of bainite laths as well as regions of twinned martensite. Area fraction of M-A constituents in these regions was 10–16%.
2. Strength of the welds was 93–97% of strength of the base material, and ductility was about 85%. Charpy impact energy of welded samples was very low at all test temperatures. High concentration of M-A constituent and residual stresses in ICHAZ, as well as a dendritic martensitic structure with carbide interlayers along the boundaries of martensite laths in FZ were the main reasons of sharp decrease in charpy impact energy of the welded samples.
3. After annealing, in ICHAZ, DUB and the regions of M-A constituents decayed forming tempered sorbite and Fe_2C and Fe_3C carbides, respectively. Also, microhardness was reduced down to 320 HV. Charpy impact energy of the welds doubled after annealing compared to welds without annealing, and DBTT decreased down to –60°C.

Declaration of competing interest

The authors declare that they have no known competing financial interests or personal relationships that could have appeared to influence the work reported in this paper.

Acknowledgments

Microstructural studies and mechanical tests of laser welds were performed within the frame of the Fundamental Research Program of the State Academies of Sciences for 2013–2020, line of research III.23.1.1. Part of the research related to the selection of optimal laser welding parameters for low carbon steels was carried out within Basic State Project No. AAAA-A17-117030610122-6.

TEM studies were carried out in Center of Federal Research Center of Kirensky Institute of Physics SB RAS. Energy dispersive analysis was carried out in NANOTECH Centre of Institute of Strength Physics and Materials Science SB RAS.

References

[1] J. Chen, S. Tang, Z.-Y. Liu, G.-D. Wang, Microstructural characteristics with various cooling paths and the mechanism of embrittlement and toughening in low-carbon high performance bridge steel, Mater. Sci. Eng. A 559 (2013) 241–249, https://doi.org/10.1016/j.msea.2012.08.091.

[2] S. Ghosh, S. Mula, Thermomechanical processing of low carbon Nb–Ti stabilized microalloyed steel: microstructure and mechanical properties, Mater. Sci. Eng. A 646 (2015) 218–233, https://doi.org/10.1016/j.msea.2015.08.072.

[3] X.L. Yang, X.D. Tan, Y.B. Xu, Z.P. Hu, Y.M. Yu, D. Wu, Effect of rolling process on impact toughness in high strength low carbon bainitic steel, Mater. Sci. Forum 816 (2015) 743–749. https://doi.org/10.4028/www.scientific.net/MSF.816.743.

[4] V.V. Natarajan, S. Liu, V.S.A. Challa, R.D.K. Misra, D.M. Sidorenko, M. D. Mulholland, M. Manohar, J.E. Hartmann, Processing-structure-mechanical property relationship in Ti-Nb microalloyed steel: continuous cooling versus interrupted cooling, Mater. Sci. Eng. A 671 (2016) 254–263, https://doi.org/10.1016/j.msea.2016.06.061.

[5] T. Jia, Y. Zhou, X. Jia, Z. Wang, Effects of microstructure on CVN impact toughness in thermomechanically processed high strength microalloyed steel, Metall. Mater. Trans. A 48 (2017) 685–696, https://doi.org/10.1007/s11661-016-3893-9.

[6] R. Maksuti, H. Mehmeti, H. Baum, M. Rama, N. Çerkini, Correlation of microstructure and toughness of the welded joint of pipeline steel X65, in: Damage Fract. Mech, Springer Netherlands, Dordrecht, 2009, pp. 315–322, https://doi.org/10.1007/978-90-481-2669-9_33.

[7] L.A. Efimenko, T.S. Esiev, D.V. Ponomarenko, S.P. Sevast'yanov, I.Y. Utkin, Effect of heat treatment on impact strength of welded joint metal made by submerged-arc welding, Metallurgist 62 (2018) 254–260, https://doi.org/10.1007/s11015-018-0653-7.

[8] D. Kong, C. Ye, W. Guo, Y. Wu, D. Long, Microstructures and plane energy spectra of X80 pipeline steel welded joints by submerged arc automatic welding, J. Wuhan Univ. Technol. Sci. Ed. 29 (2014) 1265–1269, https://doi.org/10.1007/s11595-014-1079-0.

[9] J.H. Lee, S.H. Park, H.S. Kwon, G.S. Kim, C.S. Lee, Laser, tungsten inert gas, and metal active gas welding of DP780 steel: comparison of hardness, tensile properties and fatigue resistance, Mater. Des. 64 (2014) 559–565, https://doi.org/10.1016/j.matdes.2014.07.065.

[10] S. Němeček, T. Mužík, M. Míšek, Differences between laser and arc welding of HSS steels, Phys. Procedia. 39 (2012) 67–74, https://doi.org/10.1016/j.phpro.2012.10.015.

[11] Q. Jia, W. Guo, W. Li, P. Peng, Y. Zhu, G. Zou, Y. Peng, Z. Tian, Experimental and numerical study on local mechanical properties and failure analysis of laser welded DP980 steels, Mater. Sci. Eng. A 680 (2017) 378–387, https://doi.org/10.1016/j.msea.2016.10.121.

[12] X.-N. Wang, C.-J. Chen, H.-S. Wang, S.-H. Zhang, M. Zhang, X. Luo, Microstructure formation and precipitation in laser welding of microalloyed C–Mn steel, J. Mater. Process. Technol. 226 (2015) 106–114, https://doi.org/10.1016/j.jmatprotec.2015.07.010.

[13] W. Li, L. Ma, P. Peng, Q. Jia, Z. Wan, Y. Zhu, W. Guo, Microstructural evolution and deformation behavior of fiber laser welded QP980 steel joint, Mater. Sci. Eng. A 717 (2018) 124–133, https://doi.org/10.1016/j.msea.2018.01.050.

[14] A. Malikov, A. Orishich, A. Golyshev, E. Karpov, Manufacturing of high-strength laser welded joints of an industrial aluminum alloy of system Al-Cu-Li by means of post heat treatment, J. Manuf. Process. 41 (2019) 101–110, https://doi.org/10.1016/J.JMAPRO.2019.03.037.

[15] S. Pallaspuro, A. Kaijalainen, S. Mehtonen, J. Kömi, Z. Zhang, D. Porter, Effect of microstructure on the impact toughness transition temperature of direct-quenched steels, Mater. Sci. Eng. A 712 (2018) 671–680, https://doi.org/10.1016/j.msea.2017.12.037.

[16] S. Zajac, V. Schwinn, K.H. Tacke, Characterisation and quantification of complex bainitic microstructures in high and ultra-high strength linepipe steels, Mater. Sci. Forum 500–501 (2005) 387–394. https://doi.org/10.4028/www.scientific.net/MSF.500-501.387.

[17] X. Li, C. Shang, X. Ma, S.V. Subramanian, R.D.K. Misra, J. Sun, Structure and crystallography of martensite–austenite constituent in the intercritically reheated coarse-grained heat affected zone of a high strength pipeline steel, Mater. Char. 138 (2018) 107–112, https://doi.org/10.1016/j.matchar.2018.01.042.

[18] X. Luo, X. Chen, T. Wang, S. Pan, Z. Wang, Effect of morphologies of martensite–austenite constituents on impact toughness in intercritically reheated coarse-grained heat-affected zone of HSLA steel, Mater. Sci. Eng. A 710 (2018) 192–199, https://doi.org/10.1016/j.msea.2017.10.079.

[19] C. Li, Y. Wang, T. Han, B. Han, L. Li, Microstructure and toughness of coarse grain heat-affected zone of domestic X70 pipeline steel during in-service welding, J. Mater. Sci. 46 (2011) 727–733, https://doi.org/10.1007/s10853-010-4803-y.

[20] X.-J. Di, L. Cai, X.-X. Xing, C.-X. Chen, Z.-K. Xue, Microstructure and mechanical properties of intercritical heat-affected zone of X80 pipeline steel in simulated in-service welding, Acta Metall. Sin. (English Lett. 28 (2015) 883–891, https://doi.org/10.1007/s40195-015-0272-2.

[21] P.M. Kelly, A. Jostsons, R.G. Blake, The orientation relationship between lath martensite and austenite in low carbon, low alloy steels, Acta Metall. Mater. 38 (1990) 1075–1081, https://doi.org/10.1016/0956-7151(90)90180-O.

[22] X. Li, X. Ma, S.V. Subramanian, C. Shang, R.D.K. Misra, Influence of prior austenite grain size on martensite–austenite constituent and toughness in the heat affected zone of 700MPa high strength linepipe steel, Mater. Sci. Eng. A 616 (2014) 141–147, https://doi.org/10.1016/j.msea.2014.07.100.

[23] L. Lan, C. Qiu, D. Zhao, X. Gao, L. Du, Analysis of martensite–austenite constituent and its effect on toughness in submerged arc welded joint of low carbon bainitic steel, J. Mater. Sci. 47 (2012) 4732–4742, https://doi.org/10.1007/s10853-012-6346-x.

[24] X. Li, C. Shang, X. Ma, S.V. Subramanian, Study on the toughness of X100 pipeline steel heat affected zone, in: Energy Mater. 2014, Springer International Publishing, Cham, 2014, pp. 597–604, https://doi.org/10.1007/978-3-319-48765-6_72.

[25] O.M. Akselsen, Ø. Grong, J.K. Solberg, Structure–property relationships in intercritical heat affected zone of low-carbon microalloyed steels, Mater. Sci. Technol. 3 (1987) 649–655, https://doi.org/10.1179/mst.1987.3.8.649.

[26] W. Guo, Z. Wan, P. Peng, Q. Jia, G. Zou, Y. Peng, Microstructure and mechanical properties of fiber laser welded QP980 steel, J. Mater. Process. Technol. 256 (2018) 229–238, https://doi.org/10.1016/J.JMATPROTEC.2018.02.015.

[27] L.S. Derevyagina, A.I. Gordienko, Y.I. Pochivalov, A.S. Smirnova, Modification of the structure of low-carbon pipe steel by helical rolling, and the increase in its strength and cold resistance, Phys. Met. Metallogr. 119 (2018) 83–91, https://doi.org/10.1134/S0031918X18010076.

[28] Y. Zhou, T. Jia, X. Zhang, Z. Liu, R.D.K. Misra, Investigation on tempering of granular bainite in an offshore platform steel, Mater. Sci. Eng. A 626 (2015) 352–361, https://doi.org/10.1016/j.msea.2014.12.074.